White Rose Research Online

eprints@whiterose.ac.uk
https://eprints.whiterose.ac.uk
Universities of Leeds, Sheffield and York

Deposited via The University of Sheffield.

White Rose Research Online URL for this paper:
https://eprints.whiterose.ac.uk/id/eprint/93733/

Version: Accepted Version

Article:
Kästner, M., Metsch, P. and de Borst, R. (2016) Isogeometric analysis of the Cahn-Hilliard equation - a convergence study. Journal of Computational Physics, 305. pp. 360-371. ISSN: 0021-9991

https://doi.org/10.1016/j.jcp.2015.10.047

Article available under the terms of the CC-BY-NC-ND licence (https://creativecommons.org/licenses/by-nc-nd/4.0/)

Reuse
Items deposited in White Rose Research Online are protected by copyright, with all rights reserved unless indicated otherwise. They may be downloaded and/or printed for private study, or other acts as permitted by national copyright laws. The publisher or other rights holders may allow further reproduction and re-use of the full text version. This is indicated by the licence information on the White Rose Research Online record for the item.

Takedown
If you consider content in White Rose Research Online to be in breach of UK law, please notify us by emailing eprints@whiterose.ac.uk including the URL of the record and the reason for the withdrawal request.

Isogeometric analysis of the Cahn-Hilliard equation – a convergence study

Markus Kästner[a,b,*], Philipp Metsch[a], René de Borst[c]

[a] *Institute of Solid Mechanics, TU Dresden, 01062 Dresden, Germany*
[b] *Dresden Center for Computational Materials Science (DCMS), TU Dresden, 01062 Dresden, Germany.*
[c] *School of Engineering, University of Glasgow, Oakfield Avenue, Glasgow G12 8LT, UK*

Abstract

Herein, we present a numerical convergence study of the Cahn-Hilliard phase-field model within an isogeometric finite element analysis framework. Using a manufactured solution, a mixed formulation of the Cahn-Hilliard equation and the direct discretisation of the weak form, which requires a C^1-continuous approximation, are compared in terms of convergence rates. For approximations that are higher than second-order in space, the direct discretisation is found to be superior. Suboptimal convergence rates occur when splines of order $p = 2$ are used. This is validated with a priori error estimates for linear problems. The convergence analysis is completed with an investigation of the temporal discretisation. Second-order accuracy is found for the generalised-α method. This ensures the functionality of an adaptive time stepping scheme which is required for the efficient numerical solution of the Cahn-Hilliard equation. The isogeometric finite element framework is eventually validated by two numerical examples of spinodal decomposition.

Keywords: Cahn-Hilliard equation, isogeometric analysis, Bézier extraction, manufactured solutions

1. Introduction

Phase-field models have become a powerful tool for the modelling of phase transformations and morphological changes in different fields of physics as well as materials and engineering science. Compared to sharp-interface models their advantage is that topological changes are avoided, since interfaces are treated in a diffuse manner which is achieved through a parameter which varies continously. This phase-field parameter accounts for the different material phases and/or the concentration of the different components. Such an approach allows to fully capture the physics of the individual interfaces without the need to explicitly track them. Typical applications include the modelling and simulation of solidification processes, spinodal decomposition, coarsening of precipitate phases, shape memory effects, re-crystallisation, and dislocation dynamics [1, 2, 3, 4]. Phase-field models have been successfully applied to predict microstructural changes under external fields [5, 6], model tumor growth [7, 8, 9], and image impainting [10]. The phase-field approach has also been used to model crack propagation [11, 12, 13, 14, 15].

Different numerical techniques have been utilised to solve the governing equations of phase-field models [16], including finite difference, finite element, and spectral methods. A difficulty regarding the solution of phase-field models is that they typically involve spatial differential operators that are higher than second-order. Therefore, standard finite elements based on C^0-continuous Lagrangian polynomial shape functions do not provide converging solutions when directly applied to the phase-field equation. Instead, mixed formulations [17, 18], where the governing equations are split into a coupled system of lower-order differential equations, can be used. However, this approach introduces additional unknowns and is prone to stability issues [19, 20]. Alternatively, Wells et al. [21] have combined features of continuous and discontinuous Galerkin methods, cf. [22], to use a lower-order continuity basis than is actually required by the weak form. Hence, C^0-continuous Lagrangian basis functions can be used, while the first-order inter-element continuity is weakly enforced by Nitsche's method. Although efficient as no additional unknowns are

*Corresponding author. Tel.: +49 351 46332656.
Email addresses: markus.kaestner@tu-dresden.de (Markus Kästner), philipp.metsch@tu-dresden.de (Philipp Metsch), rene.deborst@glasgow.ac.uk (René de Borst)

introduced, the approach changes the assembly procedures for the global system of equations and requires a careful choice of the penalty parameter. Starting with the work of Gómez [23] a new approach to the numerical modelling of structural evolution processes has emerged, which combines phase-field models with spline-based approximations. Such an isogeometric analysis framework allows for an accurate and efficient resolution of steep gradients that can occur when higher-order derivatives are introduced. Moreover, the higher-order continuity that is provided by these approximations allows for a direct discretisation without additional degrees of freedom. Different from earlier approaches based on Hermite elements [24, 25] it can straightforwardly be applied to two- and three-dimensional problems.

Analytic solutions for multidimensional phase-field problems are generally not available. For this reason, the comparison of different discretisations in terms of a quantitive convergence analysis is cumbersome. Approaches commonly use linearised or one-dimensional models in order to carry out accuracy tests. Alternatively, the numerical result that stems from the finest discretisation is considered as the reference solution [26]. Zhang et al. [27] have presented a convergence analysis based on the method of manufactured solutions [28]. By assuming an appropriate solution and extending the underlying differential equation by a source term, different discretisations of the same phase-field model can be compared, see also Aristotelous et al. [29] and Kay et al. [30]. To the authors' knowledge a quantitative convergence study for diffuse interface models has never been carried out within the framework of isogeometric analysis. For this reason, the Cahn-Hilliard equation is used here as a prototypical higher-order equation, and the numerical properties of different discretisations are analysed by a manufactured solution approach.

Originally derived to model spinodal decomposition of binary mixtures [31, 32], the Cahn-Hilliard equation is one of the most commonly used diffuse interface models. Taking the concentration c of one of the mixtures' components as an appropriate phase-field parameter, the governing equation can be stated as

$$\frac{\partial c}{\partial t} = \Big[M(c) \left(f'(c) - \lambda c_{,kk} \right)_{,l} \Big]_{,l} \quad . \tag{1}$$

Herein, λ is the interface parameter that governs the width of the interface which separates two adjacent phases, $M(c)$ is the concentration dependant mobility, while $(\cdot)'$ and $(\cdot)_{,k}$ designate the derivative $\partial(\cdot)/\partial c$ and the spatial derivative $\partial(\cdot)/\partial x_k$, respectively. Eventually, $f(c)$ represents the configurational or bulk free energy, which can be described by the generalised logarithmic potential [33]

$$f(c) = A \left[c \ln(c) + (1 - c) \ln(1 - c) + Bc(1 - c) \right] \tag{2}$$

with constants A and B. The bulk free energy accounts for phase separation which dominates the early stages of the evolution process. A second term, called the gradient or the interfacial free energy, contributes to the total Ginsburg-Landau free energy

$$\mathcal{F} = \mathcal{F}_{\text{bulk}} + \mathcal{F}_{\text{int}} = \int_{\Omega} \left(f(c) + \frac{\lambda}{2} c_{,k}^2 \right) \mathrm{d}V \tag{3}$$

and accounts for the influence of the individual interfaces on the system. While the total free energy $\mathcal{F}$ is minimised in the course of the structural evolution, different phenomena can occur. Both quantities, $\mathcal{F}_{\text{bulk}}$ and $\mathcal{F}_{\text{int}}$, can be used to explain these phenomena from an energetic point of view.

This paper is organised as follows: In Section 2 different finite element formulations are presented for the numerical solution of the Cahn-Hilliard problem, i.e., a mixed form and a direct approach. For the latter, approximations with at least C^1 inter-element continuity are required. In Section 3, these discretisations are compared. The numerical properties of both approaches are analysed in terms of the error norms and the convergence rates by making use of a manufactured solution. In Section 4 numerical examples for the spinodal decomposition are presented.

2. Finite element method

In this contribution, isogeometric analysis is applied to the spatial discretisation of the Cahn-Hilliard equation. The spline-based discretisations offer higher-order continuity properties and are therefore suitable for the direct discretisation of weak forms involving higher-order spatial derivatives. For the temporal discretisation, the generalised-α method [34, 35] is used. Following Gómez et al. [23], the method allows for the development of an efficient time stepping algorithm based on elementary error control. This is necessary to capture the full dynamics of the structural evolution which takes place on a time-scale varying over several orders of magnitude.

2.1. Spatial discretisation

The essential difference between the standard finite element method and isogeometric element analysis is the replacement of Lagrangian polynomials by spline basis functions, resulting in a higher-order continuity which is of interest in the present study. Similar to isoparametric finite elements, isogeometric finite element analysis uses the same Ansatz for the representation of the geometry and for the approximation of field quantities

$$\mathbf{x}(\xi) = \sum_{I=1}^{n} N_{I,p}(\xi) \boldsymbol{P}_I \tag{4}$$

$$u(\xi) = \sum_{I=1}^{n} N_{I,p}(\xi) u_I \tag{5}$$

with the univariate spline basis functions $N_{I,p}(\xi)$, the geometric control points $\boldsymbol{P}_I$, and the control values u_I of a generalised scalar primary field variable u. The term spline basis is used in the remainder when it is not necessary to distinguish between B-spline or NURBS bases. The basis functions of order p are defined by a knot vector $\boldsymbol{\Xi}$ which is a set of coordinates ξ in the parametric domain, Figure 1. This one-dimensional approximation can be generalised to surfaces and volumes by tensor products of the univariate basis functions [36, 37].

Isogeometric analysis can be implemented directly using the spline basis functions defined on patches, but it is more convenient to apply Bézier extraction [38] to map the spline basis onto a local, C^0-continuous, piecewise Bernstein polynomial basis

$$N_I\left(\bar{\xi}\right) = C_{IJ} M_J\left(\bar{\xi}\right) \quad , \tag{6}$$

see also Figure 1. The matrix $\boldsymbol{C}$ represents the Bézier extraction operator. It relates spline basis functions to the Bernstein polynomials $M_J\left(\bar{\xi}\right)$ which are functions of the element coordinate $\bar{\xi}$. Using this transformation, the original patch is decomposed into C^0-continuous Bézier finite elements, one for each non-zero knot span $[\xi_I \;\; \xi_{I+1}]$ in the original knot vector $\boldsymbol{\Xi}$. These elements can be handled in the same way as standard finite elements. While the extraction operator defined above acts between all spline basis functions and Bernstein polynomials functions of a given knot vector, a local extraction operator [38] is used in the practical implementation.

Because of the Bézier extraction, a finite element point of view is adopted for the remainder, i.e., the domain Ω is discretised into a set of n_e finite elements $\Omega = \bigcup_{I=1}^{n_\mathrm{e}} \Omega_I^\mathrm{e}$. The approximation of a generalised primary field variable u and its spatial derivatives in each element domain Ω^e are given by

$$u = \boldsymbol{N}\boldsymbol{u}, \quad u_{,k} = \boldsymbol{B}\boldsymbol{u}, \quad u_{,kk} = \boldsymbol{B}'\boldsymbol{u} \tag{7}$$

with $\boldsymbol{N}$, $\boldsymbol{B}$, and $\boldsymbol{B}'$ row vector or matrix representations of the element shape functions and their corresponding first-order and second-order spatial derivatives, respectively. The same notation is used for standard and isogeometric finite elements. All nodal or control point degrees of freedom are contained in the column vector $\boldsymbol{u}$.

2.1.1. Mixed formulation

In order to avoid the discretisation of higher-order derivatives, the Cahn-Hilliard equation can be split into a system of two second-order partial differential equations

$$\frac{\partial c}{\partial t} = \left[M(c)\mu_{,k}\right]_{,k} \tag{8a}$$

$$\mu = f'(c) - \lambda c_{,kk} \quad . \tag{8b}$$

This is done by introducing the chemical potential μ as an additional primary field variable. The corresponding weak form of the system is obtained by multiplying the Equations (8a) and (8b) by test functions w and v, respectively. Integration by parts and applying Gauss' theorem eventually lead to

$$\int_{\Omega^\mathrm{e}} \frac{\partial c}{\partial t} w \,\mathrm{d}V + \int_{\Omega^\mathrm{e}} M(c)\mu_{,k} w_{,k} \,\mathrm{d}V = \int_{\partial\Omega^\mathrm{e}} M(c)\mu_{,k} n_k w \,\mathrm{d}S \tag{9a}$$

$$\int_{\Omega^\mathrm{e}} \mu v \,\mathrm{d}V - \int_{\Omega^\mathrm{e}} f'(c) v \,\mathrm{d}V - \int_{\Omega^\mathrm{e}} \lambda c_{,k} v_{,k} \,\mathrm{d}V = -\int_{\partial\Omega^\mathrm{e}} \lambda c_{,k} n_k v \,\mathrm{d}S \quad . \tag{9b}$$

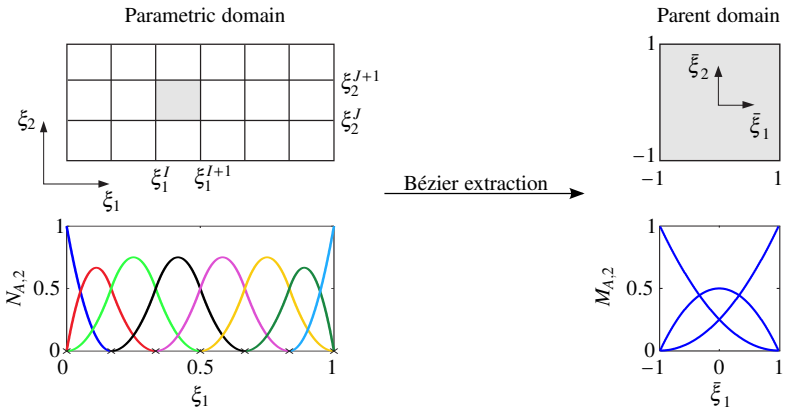

Figure 1: Spatial discretisation and geometrical mapping in isogeometric finite element analysis implemented via Bézier extraction: the parametric domain with B-spline basis functions along the ξ_1-direction and the parent domain with C^0-continuous Bernstein polynomials along the $\bar{\xi}_1$-direction. The mapping between the two domains is accomplished by the Bézier extraction operator.

As exclusively homogeneous essential and natural boundary conditions, or periodic boundary conditions are used in this paper, the boundary integrals in equations (9a) and (9b) vanish and will therefore be omitted in the remainder. Inserting the approximations (7) into the weak form and taking into consideration the arbitrariness of the control point values of the test functions, yields the following system of non-linear semidiscrete equations for each element Ω^e

$$\boldsymbol{r}^c = \int_{\Omega^e} \boldsymbol{N}^T \boldsymbol{N} \dot{\boldsymbol{c}} \, \mathrm{d}V + \int_{\Omega^e} \boldsymbol{B}^T M(c) \boldsymbol{B} \boldsymbol{\mu} \, \mathrm{d}V = \boldsymbol{0} \tag{10a}$$

$$\boldsymbol{r}^\mu = \int_{\Omega^e} \boldsymbol{N}^T \boldsymbol{N} \boldsymbol{\mu} \, \mathrm{d}V - \int_{\Omega^e} \boldsymbol{N}^T f'(c) \, \mathrm{d}V - \int_{\Omega^e} \boldsymbol{B}^T \lambda \boldsymbol{B} \boldsymbol{c} \, \mathrm{d}V = \boldsymbol{0} \quad , \tag{10b}$$

where $\boldsymbol{r}^c$ and $\boldsymbol{r}^\mu$ represent the residuals, while $\dot{\boldsymbol{c}} = \partial \boldsymbol{c} / \partial t$ replaces the partial derivative with respect to time.

2.1.2. Direct approach

The corresponding weak form for the direct discretisation of the Cahn-Hilliard equation is obtained by taking the weighted residual of Equation (1). Using integration by parts, the weak form

$$\begin{aligned} &\int_{\Omega^e} \left(\frac{\partial c}{\partial t} w + M(c) f'_{,k}(c) w_{,k} + \lambda M_{,l}(c) c_{,kk} w_{,l} + \lambda M(c) c_{,kk} w_{,ll} \right) \mathrm{d}V \\ &= \int_{\partial\Omega^e} M(c) \left(f'(c) - \lambda c_{,kk} \right)_{,l} w n_l \, \mathrm{d}S + \int_{\partial\Omega^e} \lambda M(c) c_{,kk} w_{,l} n_l \, \mathrm{d}S \end{aligned} \tag{11}$$

ensues. Different from the mixed formulation, the discretisation now requires approximations that provide C^1 inter-element continuity. Using the approximations shown in Equation (7) and taking into account the choice of boundary conditions which causes the boundary integrals in Equation (11) to vanish, the semidiscrete formulation takes the form

$$\boldsymbol{r} = \int_{\Omega^e} \boldsymbol{N}^T \boldsymbol{N} \dot{\boldsymbol{c}} \, \mathrm{d}V + \int_{\Omega^e} \boldsymbol{B}^T M(c) f''(c) \boldsymbol{B} \boldsymbol{c} \, \mathrm{d}V + \int_{\Omega^e} \boldsymbol{B}^T \lambda M'(c) \boldsymbol{B}' \boldsymbol{c} \boldsymbol{B} \boldsymbol{c} \, \mathrm{d}V + \int_{\Omega^e} \boldsymbol{B}'^T \lambda M(c) \boldsymbol{B}' \boldsymbol{c} \, \mathrm{d}V = \boldsymbol{0} \quad . \tag{12}$$

with $\boldsymbol{r}$ the residual vector.

2.2. Temporal discretisation

To achieve an optimal ratio of high-frequency and low-frequency dissipation, Chung and Hulbert [34] have introduced the generalised-α method. For first-order differential equations in time, $\boldsymbol{r}(\boldsymbol{u}, \dot{\boldsymbol{u}}) = \boldsymbol{0}$, the method is given by

$$\boldsymbol{0} = \boldsymbol{r}\left(\boldsymbol{u}_{n+\alpha_\mathrm{f}}, \dot{\boldsymbol{u}}_{n+\alpha_\mathrm{m}}\right) \tag{13a}$$

$$\boldsymbol{u}_{n+1} = \boldsymbol{u}_n + \Delta t_n \dot{\boldsymbol{u}}_n + \gamma \Delta t_n \left(\dot{\boldsymbol{u}}_{n+1} - \dot{\boldsymbol{u}}_n\right) \tag{13b}$$

$$\boldsymbol{u}_{n+\alpha_\mathrm{f}} = \boldsymbol{u}_n + \alpha_\mathrm{f} \left(\boldsymbol{u}_{n+1} - \boldsymbol{u}_n\right) \tag{13c}$$

$$\dot{\boldsymbol{u}}_{n+\alpha_\mathrm{m}} = \dot{\boldsymbol{u}}_n + \alpha_\mathrm{m} \left(\dot{\boldsymbol{u}}_{n+1} - \dot{\boldsymbol{u}}_n\right) \quad . \tag{13d}$$

Here, $\Delta t_n = t_{n+1} - t_n$ represents the current time step, while the constants α_f, α_m and γ are algorithmic parameters controlling numerical dissipation. For an unconditionally stable, second-order accurate time integration scheme they can be expressed in terms of a single parameter ρ_∞ [35]

$$\alpha_\mathrm{f} = \frac{1}{1+\rho_\infty} \quad , \quad \alpha_\mathrm{m} = \frac{3-\rho_\infty}{2(1+\rho_\infty)} \quad \text{and} \quad \gamma = \frac{1}{2} + \alpha_\mathrm{m} - \alpha_\mathrm{f} \quad . \tag{14}$$

A good performance of the algorithm can be achieved by setting $\rho_\infty = 0.5$ [23, 35]. It is noted that for $\alpha_\mathrm{f} = \alpha_\mathrm{m} = \gamma = 1$, the generalised-$\alpha$ method contains the implicit Euler method as a special case.

The non-linear governing equation $\boldsymbol{r}\left(\boldsymbol{u}_{n+\alpha_\mathrm{f}}, \dot{\boldsymbol{u}}_{n+\alpha_\mathrm{m}}\right) = \boldsymbol{0}$ has to be linearised in order to solve for the field variable $\boldsymbol{u}_{n+1}$ at time t_{n+1} starting from given values $\boldsymbol{u}_n$ and $\dot{\boldsymbol{u}}_n$ at time t_n. Different from [23, 35] we take this linearisation with respect to $\boldsymbol{u}_{n+1}$ which leads to the tangent stiffness matrix

$$\boldsymbol{K} = \frac{\partial \boldsymbol{r}\left(\boldsymbol{u}_{n+\alpha_\mathrm{f}}, \dot{\boldsymbol{u}}_{n+\alpha_\mathrm{m}}\right)}{\partial \boldsymbol{u}_{n+1}} = \alpha_\mathrm{f} \frac{\partial \boldsymbol{r}\left(\boldsymbol{u}_{n+\alpha_\mathrm{f}}, \dot{\boldsymbol{u}}_{n+\alpha_\mathrm{m}}\right)}{\partial \boldsymbol{u}_{n+\alpha_\mathrm{f}}} + \frac{\alpha_\mathrm{m}}{\gamma \Delta t_n} \frac{\partial \boldsymbol{r}\left(\boldsymbol{u}_{n+\alpha_\mathrm{f}}, \dot{\boldsymbol{u}}_{n+\alpha_\mathrm{m}}\right)}{\partial \dot{\boldsymbol{u}}_{n+\alpha_\mathrm{m}}} \quad . \tag{15}$$

The factors that precede the derivatives with respect to $\boldsymbol{u}_{n+\alpha_\mathrm{f}}$ and $\dot{\boldsymbol{u}}_{n+\alpha_\mathrm{m}}$ result from the relations (13). Starting from an initialisation of the solution vector

$$\boldsymbol{u}^0_{n+1} = \boldsymbol{u}_n \tag{16a}$$

$$\dot{\boldsymbol{u}}^0_{n+1} = \frac{\gamma - 1}{\gamma} \dot{\boldsymbol{u}}_n \, , \tag{16b}$$

a Newton-Raphson algorithm based on the linearised system of equations

$$\boldsymbol{K}^{(i)} \Delta \boldsymbol{u}^{(i)}_{n+1} = \boldsymbol{r}^{(i)}\left(\boldsymbol{u}_{n+\alpha_\mathrm{f}}, \dot{\boldsymbol{u}}_{n+\alpha_\mathrm{m}}\right) \tag{17}$$

is used to determine the update of the field variable $\Delta \boldsymbol{u}^i_{n+1}$. Herein, the superscript i denotes the current iteration. After each iteration the field variables are updated

$$\boldsymbol{u}^{(i)}_{n+1} = \boldsymbol{u}^{(i-1)}_{n+1} + \Delta \boldsymbol{u}^{(i)}_{n+1} \tag{18a}$$

$$\dot{\boldsymbol{u}}^{(i)}_{n+1} = \dot{\boldsymbol{u}}^{(i-1)}_{n+1} + \frac{1}{\gamma \Delta t_n} \Delta \boldsymbol{u}^{(i)}_{n+1} \tag{18b}$$

and convergence criteria related to the norms of the residual $\boldsymbol{r}\left(\boldsymbol{u}_{n+\alpha_\mathrm{f}}, \dot{\boldsymbol{u}}_{n+\alpha_\mathrm{m}}\right)$ and of the change in $\boldsymbol{u}_{n+1}$ are checked.

As the processes involved in spinodal decomposition proceed at different time scales, an adaptive time stepping scheme has to be adopted for an efficient numerical solution. In this work, the algorithm proposed by Gómez et al. in [23] is employed. Since the generalised-α (GA) method contains the backward Euler (BE) method as a special case, it is possible to produce second-order accurate results $\boldsymbol{u}^{\mathrm{GA}}_{n+1}$ as well as first-order accurate results $\boldsymbol{u}^{\mathrm{BE}}_{n+1}$ in order to estimate the local error from

$$\varepsilon = \frac{\left\| \boldsymbol{u}^{\mathrm{GA}}_{n+1} - \boldsymbol{u}^{\mathrm{BE}}_{n+1} \right\|_\infty}{\left\| \boldsymbol{u}^{\mathrm{GA}}_{n+1} \right\|_\infty} \quad . \tag{19}$$

By setting an admissible tolerance ε^{adm} and a safety factor θ with preferably $\theta < 1$ [39], the new step size Δt_n^{new} can be computed from the current one Δt_n^{old} according to

$$\Delta t_n^{\text{new}} = \left(\frac{\theta \varepsilon^{\text{adm}}}{\varepsilon} \right)^{\frac{1}{2}} \Delta t_n^{\text{old}} \quad . \tag{20}$$

This elementary error control allows to keep ε close to ε^{adm}. If the estimated error of a computed solution exceeds the chosen tolerance, the current time step is rejected and recomputed with adapted step size. In the present simulations, a tolerance $\varepsilon^{\text{adm}} = 10^{-3}$ and a safety coefficient $\theta = 0.85$ have been used.

3. Convergence analysis based on a manufactured solution

In this section the properties of the presented FE formulations are compared for different approximations in terms of a quantitative analysis of error levels and convergence rates. As no analytical solution is available, a manufactured solution [27, 30] is utilised. The general idea is to use an arbitrary function as analytic reference solution. Since this function will normally not fulfill the governing differential equations exactly, a residual has to be added to the right hand side of the discrete system of equations. Due to the non-linearity of the problem, optimal convergence rates available for the linear case can only serve as an indicator. However, as there are no discontinuities and as a smooth free energy functional is used, these rates should be recovered fairly well.

Herein, a manufactured solution is used which varies harmonically with respect to space and time. Taking α, β and δ as constants, it is described by

$$\hat{c}(x_k, t) = \cos(\alpha \pi x_1) \cos(\beta \pi x_2) \cos(\delta \pi t) \quad . \tag{21}$$

In order to handle concentrations $c \in [-1, 1]$ which are possible with the solution (21), the polynomial free energy

$$f(c) = \frac{1}{4}(1 - c^2)^2 \tag{22}$$

is used instead of Equation (2). Evaluating the Cahn-Hilliard equation (1) for the manufactured solution (21) and assuming a constant mobility yields

$$\frac{\partial \hat{c}}{\partial t} - \left[M \left(f'(\hat{c}) - \lambda \hat{c}_{,kk} \right)_{,l} \right]_{,l} = Q(x_k, t) \tag{23}$$

with the residual

$$\begin{aligned} Q(x_k, t) = &- \cos(\alpha \pi x_1) \cos(\beta \pi x_2) \Big\{ \delta \pi \sin(\delta \pi t) + M \pi^2 \cos(\delta \pi t) \Big[\alpha^2 + \beta^2 - \lambda \pi^2 \left(\alpha^2 + \beta^2 \right)^2 + 3 \cos^2(\delta \pi t) \cdot \ldots \\ &\ldots \cdot \Big(\alpha^2 \cos^2(\beta \pi x_2) \left(2 \sin^2(\alpha \pi x_1) - \cos^2(\alpha \pi x_1) \right) \beta^2 \cos^2(\alpha \pi x_1) \left(2 \sin^2(\beta \pi x_2) - \cos^2(\beta \pi x_2) \right) \Big) \Big] \Big\} \quad . \end{aligned} \tag{24}$$

In the convergence studies carried out for the spatial and temporal discretisations this residual represents an external body load, which is completely defined in terms of the manufactured solution (21).

For the convergence analysis a set of boundary conditions has to be defined. In isogeometric analysis, the non-interpolatory nature of the shape functions does not allow to directly assign values of the concentration or chemical potential to the control points. Instead, a transformation procedure is employed to compute the corresponding control point values [40]. For the mixed formulation, analytical values $\hat{c}$ are prescribed at the control points associated to the boundary $\partial\Omega$. In addition, the natural condition $c_{,k} n_k = 0$ which is compatible to $\hat{c}$ for $\alpha, \beta = 1, 2, \ldots n$ is utilised. Virtually the same procedure is applied to derive the corresponding discrete equations for the manufactured solution of the fourth-order equation (23). However, since the condition $c_{,k} n_k = 0$ is an essential condition in the direct formulation. Considering the unit square analysis domain, this condition can be applied explicitly by setting the concentration values of the first layer of interior control points to the value of the closest control point on the boundary. This approach has also been applied in the comparable case of plate bending by Kiendl et al. [43].

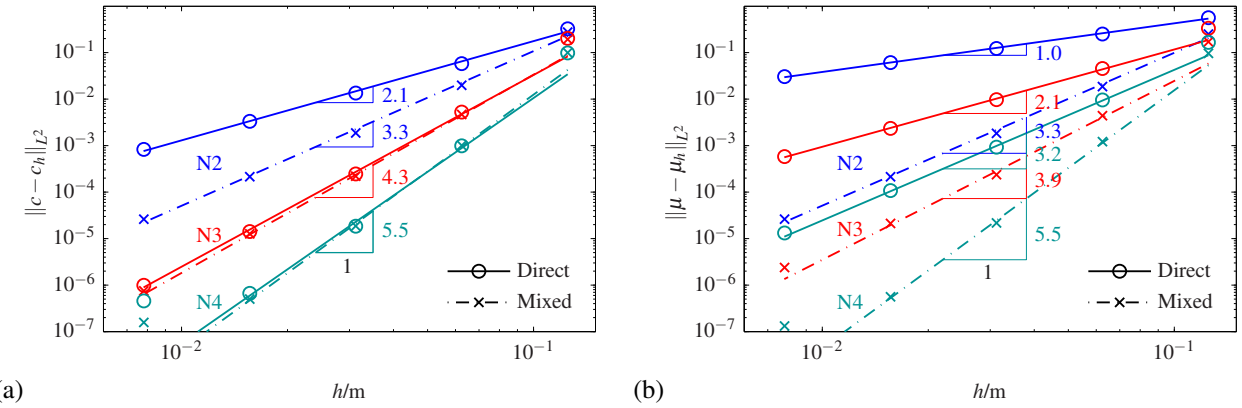

Figure 2: Quantitative comparison between the mixed formulation and the direct discretisation of the Cahn-Hilliard equation for second-order (N2), third-order (N3), and fourth-order (N4) B-splines: (a) L^2-error norm $\|c - c_h\|_{L^2}$ of the concentration c, and (b) L^2-error norm $\|\mu - \mu_h\|_{L^2}$ of the chemical potential μ as function of the element size h. In case of the direct discretisation μ is computed from $\mu = f'(c) - \lambda c_{,kk}$. Therefore, the error is governed by the H^2-error norm of the concentration field c.

3.1. Spatial discretisation

All results have been obtained using the following set of parameters: $\lambda = 0.1\,\mathrm{J\,m^{-1}}$, $M = 500\,\mathrm{m^3\,s\,kg^{-1}}$, $\alpha = \beta = 6$, and $\delta = \frac{2}{3}$. Five meshes of a unit square domain Ω with $2^n \times 2^n$ elements ($n = 3 \ldots 7$) have been considered. The focus is first put on a comparison of the performance of the mixed formulation and the direct discretisation of the Cahn-Hilliard equation. Results of isogeometric finite element analyses are shown in Figure 2. The L^2-error of the concentration field in Figure 2(a) shows a monotonic convergence for both formulations. For the mixed formulation, convergence rates are obtained which are similar to the optimal value of h^{p+1} valid for linear problems with p the order of the approximation. The results of the direct discretisation approach match the mixed formulation in terms of error levels and convergence rates for the third-order and the fourth-order approximations. For the second-order shape functions a lower convergence rate is observed for the direct approach. This is in accordance with theoretical findings for higher-order differential operators, see the discussion in Section 3.2.

For the chemical potential μ in Figure 2 (b), the two formulations are fundamentally different. The mixed approach uses the same order of approximation for c and μ and, hence, provides the same accuracy and convergence behaviour for both variables. For the direct discretisation, the chemical potential is computed from the primary field variable c according to $\mu = f'(c) - \lambda c_{,kk}$, which involves second-order derivatives. Therefore, the error of the chemical potential is governed by the H^2-error norm of the concentration field c, for which an optimal convergence rate of $p - 1$ is expected in the linear case. It is almost identically recovered by the numerical convergence study of Figure 2 (b).

In Figure 3 the same information is plotted as a function of the total number of degrees of freedom. It illustrates the fact that the direct discretisation requires less degrees of freedom to obtain a given level of accuracy. Indeed, it involves only half the number of degrees of freedom compared to the mixed formulation to achieve the same accuracy of the concentration field c, see Figure 3 (a). The less accurate approximations of the chemical potential illustrated in Figure 3 (b) are of minor importance.

Although the main motivation to apply isogeometric analysis in this case is the requirement of C^1-continuous approximations, it is also competitive when used in the mixed formulation. Figure 4 demonstrates that spline basis functions are more efficient than Lagrangian polynomials considering the total number of degrees of freedom. Moreover, the L^2-error converges at similar rates for both variants.

3.2. Convergence for higher-order linear partial differential equations

The preceding convergence study of the non-linear Cahn-Hilliard equation revealed a peculiar convergence behaviour for quadratic splines in the L^2-error norm, i.e., an order of convergence of approximately p rather than the expected value of $p + 1$. In fact, an a priori error estimate for linear, second-order and higher-order partial differential equations can be derived using the Aubin-Nitsche argument [41, 42]

$$\|u - u_h\|_{H^\sigma} \leq C_\sigma h^\beta \|u\|_{H^r} \tag{25}$$

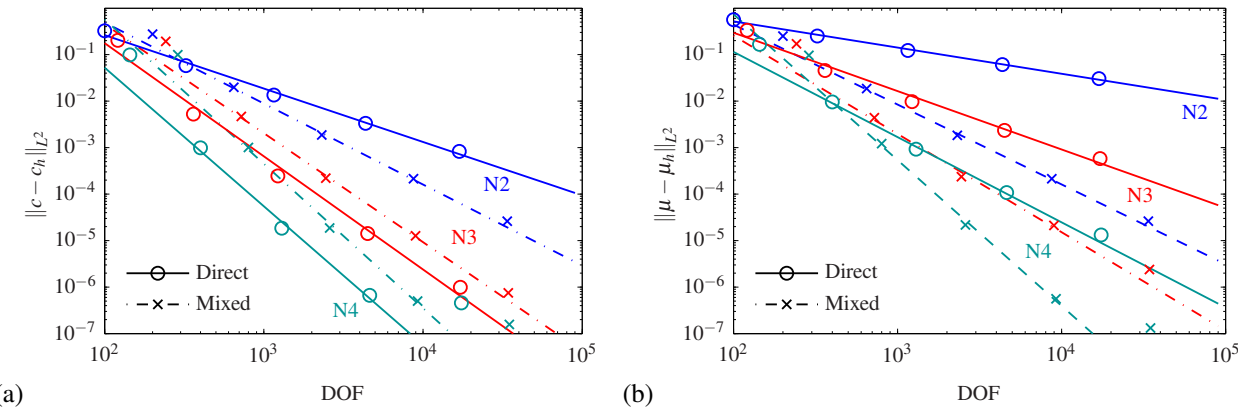

Figure 3: Quantitative comparison between the mixed formulation and the direct discretisation of the Cahn-Hilliard equation for second-order (N2), third-order (N3), and fourth-order (N4) B-splines as function of the total number of degrees of freedom (DOF): (a) L^2-error norm of the concentration c, and (b) L^2 error norm of the chemical potential μ.

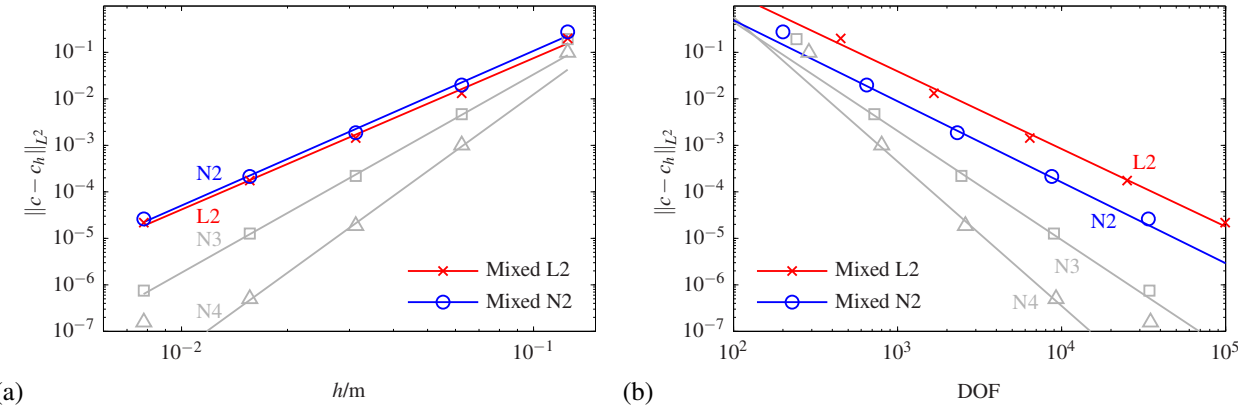

Figure 4: Quantitative comparison of the error $\|c - c_h\|_{L^2}$ between the mixed formulation discretised by quadratic Lagrangian polynomials (L2) and B-splines (N2). In addition, cubic B-splines (N3) and quartic B-splines (N4) are plotted: (a) L^2-error with respect to element size h, and (b) with respect to the total number of degrees of freedom (DOF).

with u_h the approximate solution of the primary field variable u. It turns out that the optimal order of convergence

$$\beta = \min\{\delta - \sigma, 2(\delta - m)\} \quad \text{with} \quad \delta = \min\{p + 1, r\} \tag{26}$$

depends not only on the order of approximation p, and on the error norm H^σ, but also on the order of the partial differential equation, $2m$. For a linear fourth-order differential equation ($m = 2$) and the infinitely continuous reference solution $r = \infty$ (cf. Equation (23)), the optimal orders of convergence are:

$$\|u - u_h\|_{H^0 \equiv L^2} \leq C_0 h^{\min\{p+1,\, 2(p-1)\}} \|u\|_{H^r} \quad , \tag{27a}$$

$$\|u - u_h\|_{H^1} \leq C_1 h^{\min\{p,\, 2(p-1)\}} \|u\|_{H^r} \quad , \tag{27b}$$

$$\|u - u_h\|_{H^2} \leq C_2 h^{\min\{p-1,\, 2(p-1)\}} \|u\|_{H^r} \quad . \tag{27c}$$

For $p = 2$ these equations show that the error in the L^2 and H^1-norms actually converges with the same order of $\beta = 2$, which is in good agreement with the results of the preceding study.

3.3. Temporal Discretisation

The application of higher-order time integration schemes is essential for an efficient simulation of the structural evolution described by the Cahn-Hilliard equation. Jansen et al. [35] have proved that the generalised-α method provides second-order accuracy in time for linear problems. With regard to the adaptive time stepping scheme presented

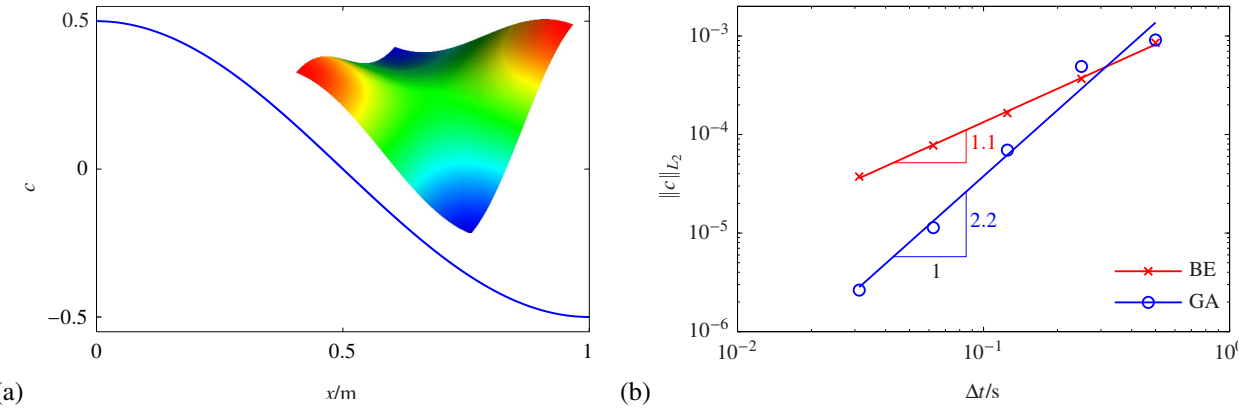

Figure 5: Quantitative comparison of time integration via backward Euler and generalised-α method: (a) plot of the adapted manufactured solution according to equation (21) with parameters $\alpha = \beta = 1$, and $\delta = \frac{2}{3}$ to avoid the influence of the spatial discretisation error, and (b) convergence of the L^2 error norm of the concentration field c with respect to the time increment Δt.

in Section 2.2, it is important that this also holds for non-linear problems. For this reason, a convergence analysis has been performed for the temporal discretisation of Equation (23).

In order to avoid interference with the spatial discretisation error, the parameters of the manufactured solution have been chosen as $\alpha = \beta = 1$ and $\delta = \frac{2}{3}$ while the unit square domain is discretised by 128×128 elements using cubic B-splines ($p = 3$). The mobility and the interface parameters are set to $M = 1\,\mathrm{m^3\,s\,kg^{-1}}$ and $\lambda = 0.1\,\mathrm{J\,m^{-1}}$, respectively. Considering a total time of $t = 0.5\,\mathrm{s}$, Equation (23) is solved five times in 2^n time steps ($n = 0 \dots 4$). The convergence behaviour of different temporal discretisations is shown in Figure 5. Results for the generalised-α method are complemented by those for the implicit Euler method. For both methods, the convergence rates match the optimal value Δt^p, as can be observed for the L^2-error norm of the concentration c. However, the accuracy obtained by the generalised-α method is significantly higher. Therefore, the error control according to Equation (20) should produce reasonable results.

4. Numerical examples

In the following examples the predictions of the mixed formulation and the discretisation for the spinodal decomposition of binary systems will be compared. As the different stages of the structural evolution can be identified by the free energy and its individual parts, special attention is paid to them. Starting from an initial concentration distribution in which small perturbations promote the evolution of the system, each problem is considered until a steady state is reached.

The course of the decomposition is influenced by the initial concentration distribution. Considering the averaged concentration in a small region $\bar{c}$, different morphologies can occur [23, 33]. While $\bar{c} = 0.5$ leads to deeply interconnected phases, values of $\bar{c} \neq 0.5$ favor one phase and result in nucleation phenomena. Moreover, the choice of a degenerate mobility

$$M(c) = Dc\,(1 - c) \tag{28}$$

with a positive constant D has a significant influence on the coarsening behaviour of the system, as it prevents the evolution of pure phases. In the simulation, the domain of interest has been taken as $1\,\mathrm{m} \times 1\,\mathrm{m}$ and is discretised into 128×128 elements with a cubic B-spline basis ($p = 3$). Considering a free energy according to equation (2), the following set of parameters is assumed: $A = 3000\,\mathrm{J}$, $B = 3$, $D = 1\,\mathrm{m^3\,s\,kg^{-1}}$, $\lambda = 1\,\mathrm{J\,m^{-1}}$.

Depending on the discretisation, the imposition of periodic boundary conditions intended for the subsequent simulation requires some consideration. In the mixed formulation, the periodicity of the two primary field variables c and μ can be imposed by constraining their control values at opposite edges of the boundary, i.e., setting $c_1 = c_n$ and $\mu_1 = \mu_n$. For the direct discretisation periodicity has to be ensured for the concentration c and its normal derivative $c_k n_k$. The direct imposition of these conditions is achieved by setting $c_I^{\mathrm{per}} = c_{n-p+I}^{\mathrm{per}}$ for $I = 1 \dots p$ and the periodic

basis functions

$$\boldsymbol{N}^{\mathrm{per}}(\bar{\xi}) = \boldsymbol{T}^{\mathrm{per}}\boldsymbol{N}(\bar{\xi}) = \boldsymbol{T}^{\mathrm{per}}\boldsymbol{C}\boldsymbol{M}(\bar{\xi}) = \boldsymbol{C}^{\mathrm{per}}\boldsymbol{M}(\bar{\xi}) \tag{29}$$

with the periodic transformation matrix $\boldsymbol{T}^{\mathrm{per}}$ and the periodic Bézier extraction operator $\boldsymbol{C}^{\mathrm{per}}$ [45].

4.1. Stochastic concentration distribution

Firstly, an initially stochastic concentration distribution $c = \bar{c} + r$ is considered with mean value $\bar{c} = 0.63$ and standard deviation $r = 0.005$. Since $\bar{c}$ is a constant, the characteristics of the evolution will be the same, locally and globally. In view of the above considerations and taking into account that periodic boundary conditions are applied, it is anticipated that in the steady state only one circular inclusion remains.

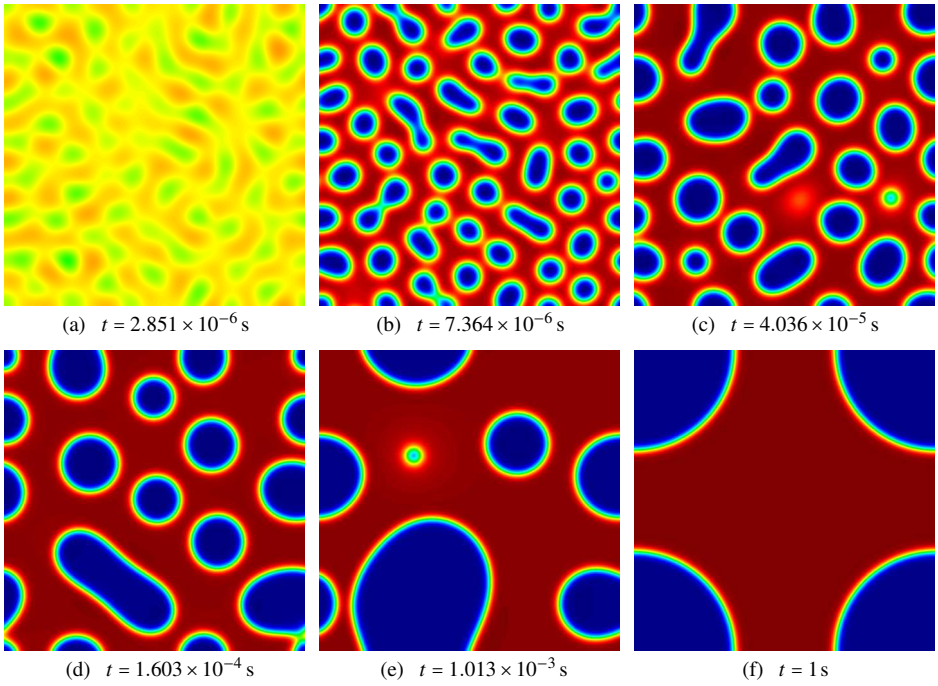

(a) $t = 2.851 \times 10^{-6}$ s (b) $t = 7.364 \times 10^{-6}$ s (c) $t = 4.036 \times 10^{-5}$ s

(d) $t = 1.603 \times 10^{-4}$ s (e) $t = 1.013 \times 10^{-3}$ s (f) $t = 1$ s

Figure 6: Spinodal decomposition from a stochastic concentration distribution with $\tilde{c} = 0.63$: temporal evolution of an initially stochastic concentration distribution into phases of different composition.

Figure 6 shows the progress of the structural evolution. From its initial concentration distribution the system separates into two phases whose composition is determined by the minima of the bulk free energy (2) which are called binodal points. This process is very fast and leads to a considerable reduction of the bulk free energy as can be seen in Figure 7 (a), which presents the temporal evolution of $\mathcal{F}$ and its individual parts $\mathcal{F}_{\mathrm{bulk}}$ and $\mathcal{F}_{\mathrm{int}}$. The figure also shows that the formation of interfacial regions is accompanied by an increase of the gradient energy – the instant of time where $\mathcal{F}_{\mathrm{int}}$ reaches its maximum value therefore marks the end of the decomposition. Subsequently, the evolution is dominated by coarsening which takes place over several magnitudes of time. In this process, the inclusions interact locally in order to minimise the gradient energy by reducing the number while increasing their characteristic length. Each decline of $\mathcal{F}_{\mathrm{int}}$ in Figure 7 (a) is related to such an interaction. The circular shape of the single inclusion that results is an outcome of the minimisation procedure.

Figure 7 (a) reveals that the total free energy decreases monotonically during the structural evolution. This is a basic property of the Cahn-Hilliard model, because $\mathcal{F}$, characterised by Equation (3), is a Lyapunov functional. Moreover, conservation of mass is used to derive the Cahn-Hilliard equation. As a consequence, the average concentration $\tilde{c}$ calculated by numerical integration should remain constant throughout the simulation. In compliance with this requirement, the variation in the temporal evolution of $\tilde{c}$ in Figure 7 (a) is not noticeable. Essentially the same characteristics of $\mathcal{F}$ and $\tilde{c}$ are found for the mixed formulation and the direct discretisation.

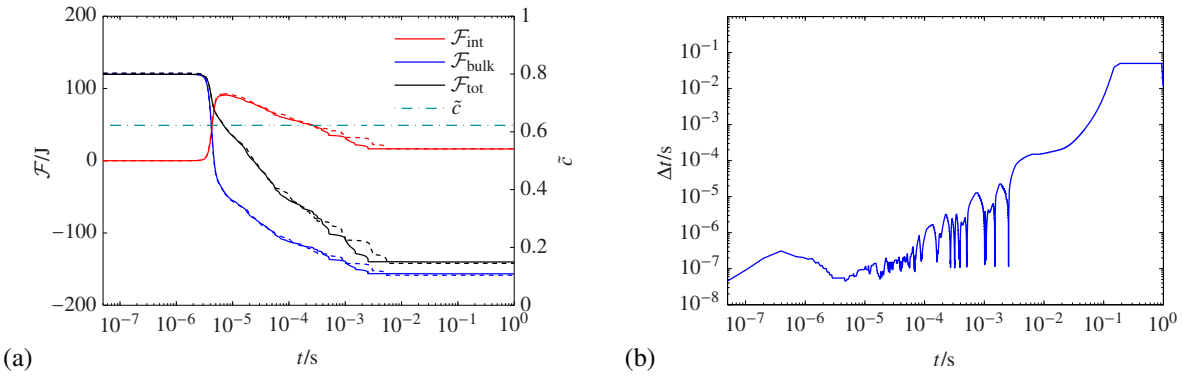

Figure 7: Spinodal decomposition from a stochastic concentration distribution with $\bar{c} = 0.63$: (a) Temporal evolution of $\bar{c}$ and $\mathcal{F}$ compared for the direct (solid lines) and mixed (dashed lines) formulation of the Cahn-Hilliard equation, and (b) evolution of the adaptively controlled time step.

An important feature of the simulation is the adaptive time stepping scheme. According to Figure 7 (b) the step size Δt ranges from $\Delta t = 5 \times 10^{-8}$ s to $\Delta t = 5 \times 10^{-2}$ s. This can only be achieved if the time step increases when the evolution shows low activity and decreases in case of larger structural changes. For this reason, every major decrease in the size of Δt corresponds to a variation of the systems structure. This is particularly obvious when comparing Figures 6 (c) – 6 (e) to Figure 7 (b). A total of 2042 time steps were needed to complete the simulation. On top of that 253 steps, which is fewer than 12 %, have been rejected in order to keep the estimated error close to the chosen tolerance $\varepsilon^{\mathrm{adm}}$. With an average of 4 Newton iterations per time step the computational effort is significantly lower than in an approach with constant step size while the results are comparable to those presented in [23, 33] for a second-order accurate time integration.

4.2. Linear concentration distribution

The purpose of the second example is to show the evolution of different morphologies as a function of the local average concentration $\bar{c}$. Therefore, an initial distribution $c = \bar{c} + r$ is considered, with $-0.005 \leq r \leq 0.005$, which represents a random perturbation to promote the evolution of the system. Herein, $\bar{c} = x_1$, $0 \leq x_1 \leq 1$, is a concentration which varies linearly in the x_1-direction. For this reason, regions with different characteristics of the evolution should develop that can be distinguished clearly [26]. As the average of the concentration is $\bar{c} = 0.5$ and homogeneous Neumann boundary conditions are applied, the steady state of the system is expected to consist of two phases of an equilibrium composition, separated by a straight interface at $x_1 = 0.5$ m.

The progress of the evolution is depicted in Figure 8 for six representative times. Again, the period of time needed for the separation process is very short. In contrast to the first example, the separation process emanates from regions where $\bar{c} \approx 0.5$, because the degenerate mobility (28) reaches its maximum value at this concentration. Hence, an interconnected pattern evolves around $x_1 = 0.5$ m, while nucleation of one phase into the other is the dominant mechanism if the local average concentration differs considerably from $\bar{c} = 0.5$. Since the mobility decreases with an increasing level of decomposition, the structural evolution at the boundaries with $x_1 = 0$ m and $x_1 = 1$ m hardly exists.

Similar to the example presented in Section 4.1 the formation of interfacial areas leads to an increase of the gradient energy $\mathcal{F}_{\mathrm{int}}$, Figure 9. The minimisation of $\mathcal{F}_{\mathrm{int}}$ via coarsening prevails at the later stages of the evolution. While the bands forming the interconnected pattern broaden, the characteristic length of the interacting inclusions increases. Once again, every decrease in the free energy corresponds to a significant change of the structure of the system which is evident when comparing Figures 8 (c) – 8 (e) to the temporal evolution of $\mathcal{F}$ depicted in Figure 9. Eventually, the shape of the remaining interface is optimised – the curved transition zone located at $x_1 = 0.5$ m develops into a straight line.

In compliance with the theoretical aspect of $\mathcal{F}$ being a Lyapunov functional, the total free energy decreases monotonically. Furthermore, the average of the concentration $\bar{c}$ shows no variation during the entire simulation, which implies that the finite element model of the Cahn-Hilliard equation fulfills the basic requirements. A comparison of the times needed by the system to reach a steady state reveals another influence of the initial condition. Different

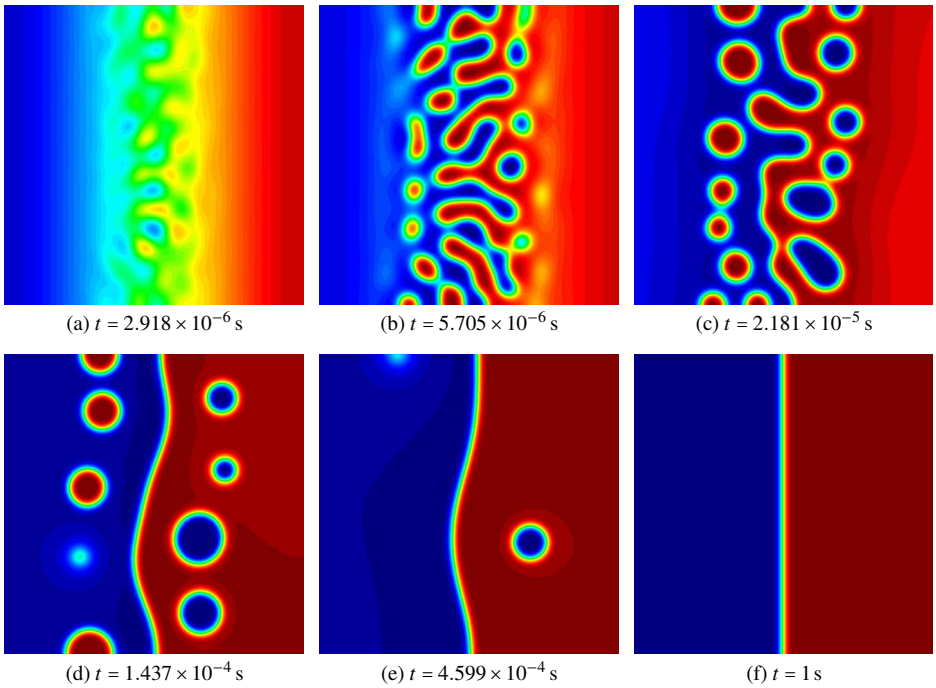

(a) $t = 2.918 \times 10^{-6}$ s (b) $t = 5.705 \times 10^{-6}$ s (c) $t = 2.181 \times 10^{-5}$ s

(d) $t = 1.437 \times 10^{-4}$ s (e) $t = 4.599 \times 10^{-4}$ s (f) $t = 1$ s

Figure 8: Spinodal decomposition from a linear, randomly perturbed concentration distribution with $\tilde{c} = 0.5$: temporal evolution of the initial concentration field into two phases separated by a straigth interface.

from the example shown in Section 4.1, the structural evolution advances much faster which is mainly caused by a smaller region of activity in the current example. The phenomenon is also in agreement with the findings in [23] where the coarsening process for deeply interconnected phases is shown to be much smoother than for droplet-type morphologies.

5. Conclusion

The present work provides a detailed convergence analysis of the Cahn-Hilliard phase-field model. Two different formulations of the model have been implemented in a Matlab-based finite element code that provides Lagrange polynomials and B-splines. Due to the lack of an analytic reference solution, the method of manufactured solutions has been adopted. With respect to the spatial discretisation, convergence rates are obtained that match analytical error estimates available for linear problems. Irrespective of the problem, the direct discretisations of higher-order partial differential equations provide superior efficiency compared to mixed formulations. However, optimal convergence rates are only obtained if approximations of sufficient order are utilised. Further investigations on the convergence behaviour of the generalised-α method justify the application of an adaptive time stepping scheme based on elementary error control. Two numerical examples of spinodal decomposition have been used to compare the physical predictions of the mixed formulation and direct discretisation approach and to validate the latter.

Ongoing research is related to the implementation of an adaptive local mesh refinement/coarsening strategy based on hierarchical B-splines. This approach allows to minimise the number of degrees of freedom of the system without affecting the accuracy. This is of special importance if large simulations of structural evolution processes are considered.

Acknowledgement

The present study is funded by the German Research Foundation (DFG), Priority Programme (SPP) 1713, grant KA 3309/3-1. This support is gratefully acknowledged. M. Kästner acknowledges financial support of the German

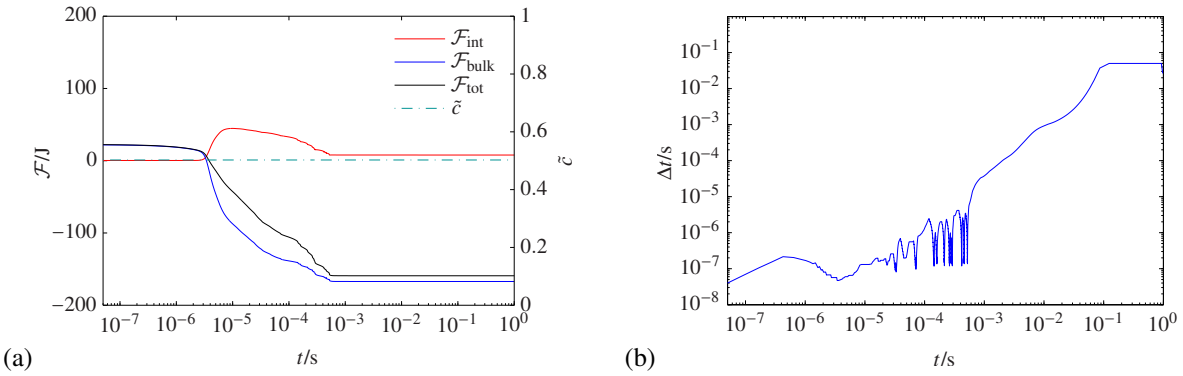

Figure 9: Spinodal decomposition from a linear, randomly perturbed concentration distribution with $\tilde{c} = 0.5$: (a) Temporal evolution of $\tilde{c}$ and $\mathcal{F}$, and (b) evolution of the adaptively controlled time step.

Academic Exchange Service (DAAD) during his research visit to the University of Glasgow.

References

[1] L.-Q. Chen, Phase-field models for microstructure evolution, Annu. Rev. Mater. Res. 32 (1) (2002) 113–140.
[2] H. Emmerich, Advances of and by phase-field modelling in condensed-matter physics, Adv. Phys. 57 (1) (2008) 1–87.
[3] N. Moelans, B. Blanpain, P. Wollants, An introduction to phase-field modeling of microstructure evolution, Calphad 32 (2) (2008) 268–294.
[4] I. Steinbach, Phase-field models in materials science, Model. Simul. Mater. Sc. 17 (7) (2009) 073001.
[5] I. Steinbach, M. Apel, The influence of lattice strain on pearlite formation in Fe-C, Acta Mater. 55 (14) (2007) 4817 – 4822.
[6] T. Koyama, Phase-field modeling of microstructure evolutions in magnetic materials, Sci. Technol. Adv. Mater. 9 (1) (2008) 013006.
[7] A. Hawkins-Daarud, K. G. van der Zee, J. Tinsley Oden, Numerical simulation of a thermodynamically consistent four-species tumor growth model, Int. J. Numer. Meth. Biomed. Engng. 28 (1) (2012) 3–24.
[8] S. M. Wise, J. S. Lowengrub, H. B. Frieboes, V. Cristini, Three-dimensional multispecies nonlinear tumor growth – I: Model and numerical method, J. Theor. Biol. 253 (3) (2008) 524 – 543.
[9] G. Vilanova, I. Colominas, H. Gomez, Capillary networks in tumor angiogenesis: From discrete endothelial cells to phasefield averaged descriptions via isogeometric analysis, Int. J. Numer. Meth. Biomed. Engng. 29 (10) (2013) 1015–1037.
[10] A. L. Bertozzi, S. Esedoglu, A. Gillette, Inpainting of Binary Images Using the Cahn-Hilliard Equation, IEEE T. Image Process. 16 (1) (2007) 285–291.
[11] C. Miehe, F. Welschinger, M. Hofacker, Thermodynamically consistent phase-field models of fracture: Variational principles and multi-field FE implementations, Int. J. Numer. Meth. Engng. 83 (10) (2010) 1273–1311.
[12] R. Spatschek, E. Brener, A. Karma, Phase field modeling of crack propagation, Philos. Mag. 91 (1) (2010) 75–95. doi:10.1080/14786431003773015.
[13] C. Kuhn, R. Müller, A continuum phase field model for fracture, Eng. Fract. Mech. 77 (18) (2010) 3625–3634.
[14] C. Hesch, K. Weinberg, Thermodynamically consistent algorithms for a finite-deformation phase-field approach to fracture, Int. J. Numer. Meth. Engng. 99 (12) (2014) 906–924.
[15] S. May, J. Vignollet, R. de Borst, A numerical assessment of phase-field models for brittle and cohesive fracture: Γ-convergence and stress oscillations, Eur. J. Mech. A-Solid. (2015) –.
[16] D. Lee, J.-Y. Huh, D. Jeong, J. Shin, A. Yun, J. Kim, Physical, mathematical, and numerical derivations of the Cahn-Hilliard equation, Comp. Mater. Sci. 81 (0) (2014) 216 – 225.
[17] C. M. Elliott, D. A. French, F. A. Milner, A second order splitting method for the Cahn-Hilliard equation, Numer. Math. 54 (5) (1989) 575–590.
[18] J. Barrett, J. Blowey, H. Garcke, Finite Element Approximation of the Cahn-Hilliard Equation with Degenerate Mobility, SIAM J. Numer. Anal. 37 (1) (1999) 286–318.
[19] F. Brezzi, On the existence, uniqueness and approximation of saddle-point problems arising from lagrangian multipliers, ESAIM: Mathematical Modelling and Numerical Analysis 8 (R2) (1974) 129–151.
URL `http://eudml.org/doc/193255`
[20] F. Brezzi, M. Fortin, Mixed and hybrid finite element methods, Springer Series in Computational Mathematics, Springer-Verlag, 1991.
[21] G. N. Wells, E. Kuhl, K. Garikipati, A discontinuous Galerkin method for the Cahn-Hilliard equation, J. Comput. Phys. 218 (2) (2006) 860–877.
[22] G. Engel, K. Garikipati, T. J. R. Hughes, M. G. Larson, L. Mazzei, R. L. Taylor, Continuous/discontinuous finite element approximations of fourth-order elliptic problems in structural and continuum mechanics with applications to thin beams and plates, and strain gradient elasticity, Comput. Methods Appl. Mech. Engrg. 191 (34) (2002) 3669–3750.
[23] H. Gómez, V. M. Calo, Y. Bazilevs, T. J. R. Hughes, Isogeometric analysis of the Cahn-Hilliard phase-field model, Comput. Methods Appl. Mech. Engrg. 197 (4950) (2008) 4333 – 4352.

[24] P. K. Chan, A. D. Rey, A numerical method for the nonlinear Cahn-Hilliard equation with nonperiodic boundary conditions, Comp. Mater. Sci 3 (3) (1995) 377–392.
[25] R. H. Stogner, G. F. Carey, B. T. Murray, Approximation of Cahn-Hilliard diffuse interface models using parallel adaptive mesh refinement and coarsening with C^1 elements, Int. J. Numer. Meth. Engng. 76 (5) (2008) 636–661.
[26] H. Gómez, A. Reali, G. Sangalli, Accurate, efficient, and (iso)geometrically flexible collocation methods for phase-field models, J. Comput. Phys. 262 (0) (2014) 153 – 171.
[27] L. Zhang, M. R. Tonks, D. Gaston, J. W. Peterson, D. Andrs, P. C. Millett, B. S. Biner, A quantitative comparison between C^0 and C^1 elements for solving the Cahn-Hilliard equation, J. Comput. Phys. 236 (0) (2013) 74 – 80.
[28] T. M. Shih, A procedure to debug computer programs, Int. J. Numer. Meth. Engng. 21 (6) (1985) 1027–1037.
URL http://dx.doi.org/10.1002/nme.1620210605
[29] A. C. Aristotelous, O. A. Karakashian, S. M. Wise, A Mixed Discontinuous Galerkin, Convex Splitting Scheme for a Modified Cahn-Hilliard Equation and an Efficient Nonlinear Multigrid Solver, Discrete Cont. Dyn.-B 18 (9) (2013) 22112238.
[30] D. Kay, V. Styles, E. Süli, Discontinuous Galerkin Finite Element Approximation of the Cahn-Hilliard Equation with Convection, SIAM J. Numer. Anal. 47 (4) (2009) 2660–2685. arXiv:http://epubs.siam.org/doi/pdf/10.1137/080726768.
[31] J. W. Cahn, J. E. Hilliard, Free Energy of a Nonuniform System. I. Interfacial Free Energy, J. Chem. Phys. 28 (2) (1958) 258–267.
[32] J. W. Cahn, Phase Separation by Spinodal Decomposition in Isotropic Systems, J. Chem. Phys. 42 (1) (1965) 93–99.
[33] O. Wodo, B. Ganapathysubramanian, Computationally efficient solution to the Cahn-Hilliard equation: Adaptive implicit time schemes, mesh sensitivity analysis and the 3D isoperimetric problem, J. Comput. Phys. 230 (15) (2011) 6037 – 6060.
[34] J. Chung, G. M. Hulbert, A Time Integration Algorithm for Structural Dynamics With Improved Numerical Dissipation: The Generalized-α Method, J. Appl. Mech. 60 (2) (1993) 371–375.
[35] K. E. Jansen, C. H. Whiting, G. M. Hulbert, A generalized-α method for integrating the filtered NavierStokes equations with a stabilized finite element method, Comput. Methods Appl. Mech. Engrg. 190 (34) (2000) 305 – 319.
[36] J. A. Cottrell, T. J. R. Hughes, Y. Bazilevs, Isogeometric Analysis: Toward Integration of CAD and FEA, John Wiley & Sons, Chichester, 2009.
[37] L. Piegl, W. Tiller, The NURBS Book, Springer-Verlag, Berlin, 1996.
[38] M. J. Borden, M. A. Scott, J. A. Evans, T. J. R. Hughes, Isogeometric finite element data structures based on Bézier extraction of NURBS, Int. J. Numer. Meth. Engng. 87 (1–5) (2011) 15–47. doi:10.1002/nme.2968.
[39] G. Söderlind, Automatic Control and Adaptive Time-Stepping, Numer. Algorithms 31 (1-4) (2002) 281–310.
[40] D. Wang, J. Xuan, An improved NURBS-based isogeometric analysis with enhanced treatment of essential boundary conditions, Comput. Methods Appl. Mech. Engrg. 199 (37–40) (2010) 2425–2436.
[41] G. Strang, G. Fix, An analysis of the finite element method, Wellesley-Cambridge Press, Wellesley, 1973.
[42] A. Tagliabue, L. Ded, A. Quarteroni, Isogeometric Analysis and error estimates for high order partial differential equations in fluid dynamics, Comput. Fluids 102 (0) (2014) 277–303.
[43] J. Kiendl, K.-U. Bletzinger, J. Linhard, R. Wüchner, Isogeometric shell analysis with Kirchhoff-Love elements, Comput. Methods Appl. Mech. Engrg. 198 (4952) (2009) 3902–3914.
[44] J. Kiendl, Y. Bazilevs, M.-C. Hsu, R. Wüchner, K.-U. Bletzinger, The bending strip method for isogeometric analysis of Kirchhoff-Love shell structures comprised of multiple patches, Comput. Methods Appl. Mech. Engrg. 199 (3740) (2010) 2403–2416.
[45] J. Liu, L. Dedè, J. A. Evans, M. J. Borden, T. J. R. Hughes, Isogeometric analysis of the advective Cahn-Hilliard equation: Spinodal decomposition under shear flow, J. Comput. Phys. 242 (0) (2013) 321–350.